The flexure-based microgap rheometer (FMR)

Christian Clasen,[a] Brian P. Gearing, and Gareth H. McKinley

Hatsopoulos Microfluids Laboratory, Massachusetts Institute of Technology, 77 Massachusetts Avenue, Cambridge, Massachusetts 02139

(Received 21 March 2006; final revision received 28 August 2006)

Synopsis

We describe the design and construction of a new microrheometer designed to facilitate the viscometric study of complex fluids with very small sample volumes (1–10 μl) and gaps of micrometer dimensions. The flexure-based microgap rheometer (FMR) is a shear-rate-controlled device capable of measuring the shear stress in a plane Couette configuration with directly controlled gaps between 1 and 200 μm. White light interferometry and a three-point nanopositioning stage using piezo-stepping motors are used to control the parallelism of the upper and lower shearing surfaces, which are constructed from glass optical flats. A compound flexure system is used to hold the fluid sample testing unit between a drive spring connected to an "inchworm" motor and an independent sensor spring. Displacements in the sensing flexure are detected using an inductive proximity sensor. Ready optical access to the transparent shearing surfaces enables monitoring of the structural evolution in the gap with a long working-distance video microscope. This configuration then allows us to determine the microgap-dependent flow behavior of complex fluids over 5 decades of shear rate. We demonstrate the capability of the FMR by characterizing the complex stress and gap-dependent flow behavior of a typical microstructured food product (mayonnaise) over the range of gaps from 8 to 100 μm and stresses from 10 to 1500 Pa. We correlate the gap-dependent rheological response to the microstructure of the emulsion and changes induced in the material by prolonged shearing. © *2006 The Society of Rheology.* [DOI: 10.1122/1.2357190]

I. INTRODUCTION

The conformational and dynamical behavior of complex fluids, polymer melts, solutions, and multiphase systems close to solid boundaries is of great interest for the polymer processing, food, and consumer products industries. In particular, when the characteristic length scale of the flow approaches microstructural scales, boundary effects such as wall slip (Barnes, 1995; Mhetar and Archer, 1998), cohesive failure (Reimers and Dealy, 1998), and adhesive failure (Migler *et al.*, 1993) occur on the same scale as the overall deformation of the bulk sample, and their impact on the measured rheological properties can no longer be neglected. These effects are especially important when structural elements (such as those encountered in self-assembling biopolymer solutions, microgels, and emulsions) dominate the viscoelastic properties of the fluid system or when

[a]Present address: Department Chemische Ingenieurstechnieken, Katholieke Universiteit Leuven, W. De Croylaan 46, 3001 Heverlee, Belgium. Author to whom correspondence should be addressed; electronic mail: Christian.Clasen@cit.kuleuven.be

characteristic microscopic length scales such as the interchain separation or the mesh spacing of a gel approach the characteristic dimension of the probe volume.

The bulk characterization of such complex fluids using conventional rheometry has always been a difficult task due to the large number of independent molecular parameters and the complex intermolecular and interfacial interactions in multiphase system such as food or consumer products. The observation of an overall or "global" rheological behavior is hard to connect to the compositional parameters of a system and often impossible to model. Furthermore, the rheological properties of the bulk sample often do not accurately represent the flow behavior of a complex fluid in the extreme situations that can occur during processing and which often limit the final properties and stability of a product. Investigations of the rheological behavior of a complex fluid on a microscopic scale are therefore of great interest and numerous different microrheometry techniques have been introduced recently.

Previous experimental configurations for microrheometry have focused primarily on either the tribological study of sliding friction in thin films or on monitoring a local rheological response using nanometer-sized particles. The nanorheological response of molecularly thin films has been studied extensively using AFM techniques (Montfort *et al.*, 1991) as well as variants of the surface force apparatus (SFA) (Israelachvili *et al.*, 1988; Giasson *et al.*, 1997; Mukhopadhyay and Granick, 2001). However, the most common geometric configuration employed in the SFA consists of mica sheets in an opposed cylinder configuration which leads to a nonhomogeneous deformation field. Numerous particle-based microrheometric techniques have also been developed over the past decade: variants include the analysis of thermally excited (or "passively driven") micron-sized particles through either diffusing wave spectroscopy (Weitz and Pine, 1992; Popescu *et al.*, 2002) or the microscopic tracking of single particles or pairs of particles (Levine and Lubensky, 2000; Starrs and Bartlett, 2003). Actively driven techniques that directly measure the forces on microscopic beads have also been developed using optical traps (Meiners and Quake, 2000; Raghu and Ananthamurthy, 2005) and magnetic tweezers (Bausch *et al.*, 1998; Gosse and Croquette, 2002). For recent reviews on the applications and interrelation of these techniques see (MacKintosh and Schmidt, 1999; Clasen and McKinley, 2004; Gardel *et al.*, 2005; Waigh, 2005).

While the techniques above probe the microrheological response on the submicron scale, many industrial processing operations, as well as the emerging field of microfluidics, lead to flows on an intermediate or "mesoscale" range (roughly spanning the range of $1-100$ μm) that cannot be readily probed with either conventional bulk rheometry or nanoscale measurements of the apparent viscosity or surface friction. With the exception of the work of Granick and co-workers (Dhinojwala and Granick, 1997; Soga *et al.*, 1998) there are few established experimental techniques that are capable of quantitatively measuring the true viscometric material functions of complex fluids under homogeneous deformation conditions on the meso- to microscales.

The aim of this paper is therefore to introduce a new instrumental design which we refer to as a flexure-based microgap rheometer (FMR). This instrument allows the determination of the viscometric properties of small fluid samples (<10 μl) using adjustable gaps that span mesoscale dimensions from 200 μm down to 1 μm. We first describe the construction and calibration of the instrument and then proceed to demonstrate its utility in studying the gap-dependent and shear-stress-dependent rheology of a typical microstructured food product.

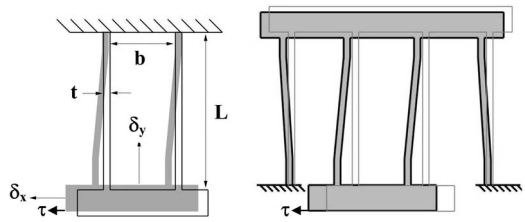

FIG. 1. Flexure systems. Left: double flexure assures a displacement δ_x, caused by a shear stress τ, without rotational movement but still results in an orthogonal displacement δ_y. Right: compound flexure compensates for orthogonal movement and allows for a purely linear displacement under action of a shear stress.

II. EXPERIMENT

A. Compound flexures

The flexure-based microgap rheometer (FMR) is a miniaturized sliding plate rheometer (Giacomin *et al.*, 1989) that generates a plane Couette shearing flow between two optical flats. One of the keys to the FMR's capability of delivering large deformations while maintaining a constant gap setting (over a range $1 \leqslant h \leqslant 200$ μm) on a micrometer scale is the compound flexure system (Gearing and Anand, 2001; Gudlavalleti *et al.*, 2005) that is used to hold the test fixtures and fluid sample between a drive spring and an independent sensor spring. The compound flexure consists of two double leafsprings that are coupled to the same independent translating frame. Using one double flexure as shown in Fig. 1(a) allows for a linear displacement without any rotational movement when acted upon by a shear stress τ. However, the displacement δ_x of the moving bar also gives rise to an orthogonal displacement δ_y. In the compound flexure this orthogonal displacement δ_y is compensated by a second, outer pair of springs [shown in Fig. 1(b)] with the same dimensions as the inner pair. Every bending movement of the inner spring assembly is mirrored by that of the outer spring and this enables purely linear relative translation over distances of several millimeters with an orthogonal displacement of less than 1 nm. The dynamic force range of the instrument is determined by the spring constant K of the flexure. This can be varied greatly by changing the length L, depth w, thickness t, and/or Young's modulus E of the compound flexures, through the beam relationship

$$K = E\left(\frac{wt^3}{L^3}\right). \tag{1}$$

Alignment fidelity, device orthogonality, and total error stack-up are all optimized by machining the entire instrument frame from a single monolithic block of aluminum with a thickness $w=25.4$ mm, using a CAD design package plus water-jet and EDM technology. The design of the compound flexure used for the FMR in this paper is shown in Fig. 2; the dimensions are $t=2.54$ mm and $L=180$ mm for the drive spring and $t=2.54$ mm and $L=80$ mm for the sensor spring, resulting in a theoretical spring constant of $K=5.0\times10^3$ N/m for the drive spring and $K=5.7\times10^4$ N/m for the sensor spring. The experimentally determined values of $K=8.1\times10^3$ N/m for the drive and 8.2×10^4 N/m for the sensor spring deviate from the theoretical values due to the nonorthogonal cuts of the weakly divergent water jet. Calibrations give a standard deviation of the linearity of the sensor spring of $<2\%$ with loads up to 8 N, corresponding to lateral displacements of less then 97 μm.

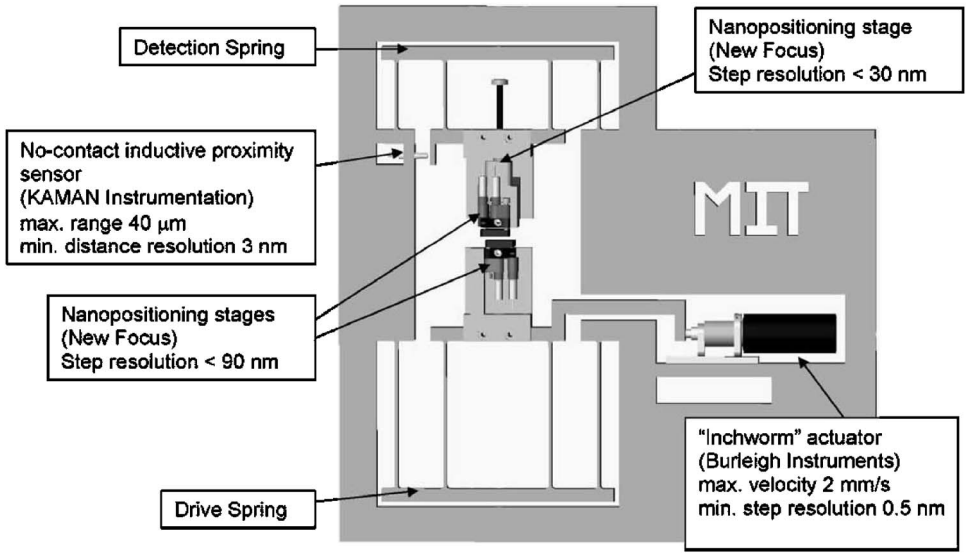

FIG. 2. Schematic view of the compound flexure, sensor-, and positioning systems of the flexure-based microgap rheometer (FMR) without the white light interferometry unit.

Finite element method (FEM) simulations have also been carried out to determine the mechanical response limits of the drive spring at the maximum orthogonal displacement of 3 mm and the maximum velocity of 2 mm/s (Gudlavalleti *et al.*, 2005). The simulations show an unlimited fatigue lifetime for the setup, no yielding at maximum deflection, and a normal force stability of the springs against buckling (over the entire displacement range) of at least 170 N.

The drive spring is driven by an "inchworm" motor (Burleigh Instruments IW-810, Victor, NY) capable of a maximum displacement of $\delta_x = 6$ mm (but limited by design in the current setup to $\delta_x = 1.6$ mm) and a step resolution of 0.5 nm, capable of speeds up to $U_{max} = 2$ mm/s.

Displacements in the sensing flexure are detected using a noninvasive inductive proximity sensor (KAMAN Instrumentation SMU 9200-5U, Colorado Springs, CO) with a resolution of ±1 nm and a maximum sensing range of 40 μm. The sensor is fixed to the outer frame and the distance is directly measured from the sensor face to the lateral moving aluminum bar of the upper flexure that serves as the "pick up" to detect shear stresses. In combination with the chosen sensor spring stiffness, it is possible to detect forces with maximum loads of up to 3.3 N with an accuracy of 0.1 mN.

B. Shearing cell

The shearing cell consists of two optical flats (Edmund Scientific, Tonawanda, NY), polished within $\lambda/20$ ($\approx \pm 30$ nm over 25 mm surface) and coated with a semireflective layer of 100 nm TiO_2. The upper flat is cut into a square shape via a diamond machining process, with the edges parallel and perpendicular to the travel direction of the inchworm actuator. The lower flat is larger than the upper flat, by at least 2 mm in the moving direction and 1 mm orthogonal to the moving direction. Both optical flats can be removed from their mounts to permit easy cleaning and to provide the possibility of using shearing surfaces with different contact areas. The use of different shearing surface areas allows us

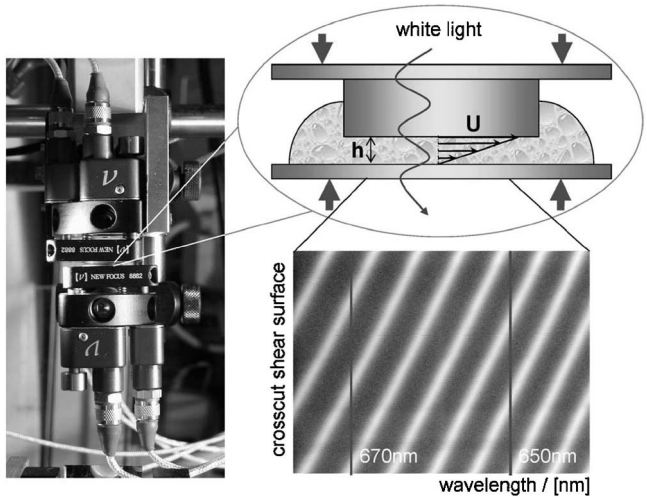

FIG. 3. White light interferometry: only integer wavelengths are transmitted through the cavity of the shearing cell with gap h (not shown to scale). A crosscut of the transmitted beam, corresponding to a section across the shearing surface, is resolved into discrete wavelengths in the spectrometer. A tilted fringe pattern arises from a spatially varying gap separation.

to adjust the range of measurable stresses as well as to enhance the rate of normal force relaxation during the sample loading process, which involves large squeezing deformations at small gaps.

The optical flats are mounted on three-point nanopositioning stages (New Focus, San Jose, CA) as shown in Fig. 3, which allow for an adjustment of the flats in two dimensions with a tilt angle resolution $<0.003°$. The lower nanopositioning stage is directly connected to the drive spring; the upper is connected to the sensor spring via a linear nanopositioning stage (New Focus, San Jose, CA) that allows for an adjustment of the gap h between the optical flats with a step resolution of $\Delta h < 30$ nm.

In contrast to the sliding plate rheometer introduced by Dealy and co-workers (Giacomin *et al.*, 1989), the shear stress is determined from the force measured with the sensor spring and the whole area of the shearing surface of the upper plate, which is completely immersed into the sample as demonstrated in the sketch of Fig. 3. Edge effects that arise from uncontrollable secondary flows at the edges of the upper surface—and that may alter the resulting fluid response—are minimized by precise machining of the edges of the optical elements that form the plates, and by using a sufficiently large surface area. Assuming that the penetration depth of any secondary flow is on the order of the gap height, even for a maximum gap of 0.1 mm the ratio of gap to the characteristic length of the square shearing surface used in the present study (25 mm) is only on the order of 0.4% and can thus be neglected in the following discussion.

The shear field is applied to the sample by imposing large triangle waves (sawtooth profiles) via the lower driven plate with a constant speed U. The programed lateral displacement is $\delta_x = Ut$, resulting in a constant shear rate $\dot{\gamma} = U/h$ for a fixed gap h. The sawtooth displacement and deformation for typical experimental conditions are shown in Fig. 4. The evolution of displacement of the upper sensor flexure and thus of the shear stress τ is also shown in Fig. 4. The device is capable of measuring the start-up of steady shear and the approach to steady state as well as large amplitude oscillatory shear flow. However, in the following we report only on steady-state values of stress, averaged over

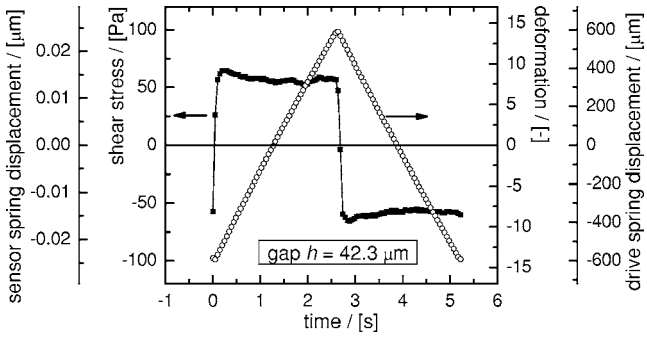

FIG. 4. Deformation and shear stress for a full cycle of the imposed sawtooth wave. Polybutadiene melt measured with a gap $h=42.3\ \mu$m and a shearing surface area of $A=20.12\ \text{mm}^2$. The speed of $U=0.225$ mm/s corresponds to a shear rate of $\dot{\gamma}=5.32\ \text{s}^{-1}$. The maximum lateral translation of $\delta_x=1.2$ mm corresponds to a deformation of $\gamma=28.35$ over a full cycle ($T=21\ ^\circ$C).

several cycles for a specified value of the shear rate. The shear strain γ was generally chosen to be large enough ($\gamma>4$) so that a constant, steady-state stress level was reached. All shear rate ramps were conducted as multiple constant rate experiments progressing from low to high shear rates.

C. White light interferometry

The parallelism of the shearing surfaces with respect to the shearing direction as well as the absolute gap separation are both controlled using the well-established technique of white light interferometry which is described in detail elsewhere (Israelachvili and Tabor, 1972; Israelachvili *et al.*, 1988; Dhinojwala and Granick, 1997; Braithwaite and McKinley, 1999). Only integer wavelengths of white light (which is projected through the gap perpendicular to the shearing direction from a fiber-coupled source) are passed through the semireflective cavity of the gap. Orthogonal 1D optical crosscuts across the shearing surfaces are dispersed by a spectrometer and the resulting fringe pattern is monitored by a CCD camera as shown in Fig. 3. The wavelength of the light emerging from the cavity at any specific point of a crosscut depends on the local gap h at this position. A progressive shift of the wavelengths resulting from two flat surfaces that are not parallel is indicated by a set of tilted fringes as shown in Fig. 3. Online processing of the fringe images, captured with a CCD camera (Cohu Inc., San Diego, CA) and an image acquisition card (PCI-1409, National Instruments Corp., Austin, TX), is performed with the IMAQ-VISION imaging software (National Instruments Corp., Austin, TX). A 2D FFT of the images (after thresholding) allows for the detection of the fringe peaks and the tilt angle. A direct closed-loop feedback adjustment of the plates to parallelism is then performed via software control of the three-point nanopositioning stages. The absolute gap h can then be calculated in terms of the known refractive index of the fluid n_f and from two fringe wavelengths λ_m and λ_{m+k} according to the following equation:

$$h=\frac{k}{2n_f}\frac{\lambda_m\lambda_{m+k}}{\lambda_m-\lambda_{m+k}},\quad k=1,2\ldots\ . \tag{2}$$

The ultimate resolution of the white light interferometry method is limited by the spectral resolution of the image acquisition system and the flatness of the optical flats which serve as shearing surfaces. Experimentally, we found that the lowest limit for the determination of gaps between optical flats with areas $>5\ \text{mm}^2$ was $1.1\pm0.2\ \mu$m. Paral-

lelism of the gap in the moving direction is indicated by constant fringe spacings, independent of the lateral position δ_x of the driven plate, and can also be simultaneously corrected using the three-point adjusts.

The optical train for white light interferometry is constructed as a separate unit and is not in direct contact with the compound spring or the shearing cell. It can be moved out of the direct access path to the optical flats by a simple sliding mechanism, and this allows for relatively easy optional installation of rheo-optical subsystems and measuring devices such as a video microscope. In principle a modulated birefringence system or light-scattering system could also be used.

D. Measurement in nontransparent media

An additional inductive proximity sensor (KAMAN Instrumentation SMU 9200-5U, Colorado Springs, CO) measures the distance between the upper and lower frames that hold the two optical flats and this yields a second, noncontacting relative measure of the sample gap. After the parallelism adjustment of the empty shearing cell a single, absolute determination of the actual gap using white light interferometry [cf. Eq. (2)], can be used to calibrate the inductive proximity sensor. The gap can then be varied over a range of 40 μm with a step distance of 30 nm with the axial linear nanopositioning stage even for nontransparent samples. Dhinojwala *et al.* report an alternate way to measure the separation and alignment of a gap via a three-point capacitance measuring technique, integrated into the shearing surfaces (Dhinojwala and Granick, 1997). In our setup the mounting of the upper plate on the axial positioning system allows for a simple and rapid separation of the aligned plates for sample loading with a repositioning accuracy of ± 0.5 μm.

E. Video microscopy

The optical access available normal to the transparent shearing surfaces enables simultaneous microscopic observation of the shearing sample in the 1-3 plane with a long working distance video microscope (K2, Infinity Photooptical-Optical, Boulder, CO) and a CCD camera (TM1, Pulnix, San Jose, CA). In the current setup, the light (with a total path length of 158 mm from sample to objective lens of the microscope) enters the sample from the quasistationary upper flat that is connected to the sensor spring. This configuration allows for the detection of particle displacement close to this surface. The video sequences are recorded at a frame rate of 30 fps and with 480×640 square pixel resolution. The spatial resolution of the resulting images is 0.54 μm/pixel.

F. Calibration and limits

The range of shear stresses that can be accessed by the instrument, as well as a comparison to rheological results of a standard bulk rheometer, are demonstrated in Fig. 5. For this purpose we use an unentangled low molar mass polybutadiene melt ($M_w = 1600$ g/mol) that exhibits Newtonian flow behavior over the observed shear rate range. The radius of gyration of the chains is much lower than the minimum gap, and no gap-dependent phenomena are to be expected. The instrument accurately measures a linear response and gap-independent shear stress over 3.5 decades of imposed deformation rate and is limited by the resolution of the inductive proximity sensor. The use of fixtures with different surface areas (see Table I) allows us to further extend the measurable range of stresses and the fluid sample volume.

In an ambient laboratory environment that is not dust free, the minimum gap is limited to $h_{min} \sim 5$ μm. Below this minimum gap setting, dust particles that are trapped between

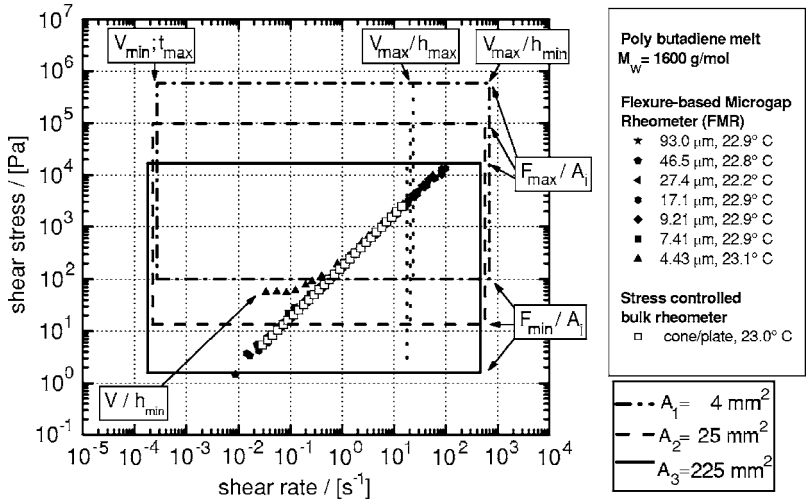

FIG. 5. Comparison of the shear-rate-dependent properties of a polybutadiene melt (M_w=1600 g/mol) in a commercial stress controlled rheometer (TA Instruments, AR1000) and the FMR.

the plates dominate the stress response below a critical shear stress. This results in a nearly constant sliding frictional stress, as can be seen in Fig. 5 for a gap of 4.43 μm and stresses below 100 Pa. In dust-free environments the minimum gap limit is ultimately determined by the spatial resolution of the white light interferometry subsystem. Giasson *et al.* show that, using mica surfaces with known thickness, gap separations in the range of a few nanometers can be measured (Giasson *et al.*, 1997). The accessible shear rate range is limited by the construction of the inchworm motor. A reliable minimum shear rate limit was experimentally confirmed to be at 2×10^{-4} s^{-1}. The upper shear rate limit corresponds to the maximum velocity of U_{max}=2 mm/s; the resulting shear rate $\dot{\gamma}_{max}=U_{max}/h$ however is also dependent on the gap setting h and lies between 20 and 400 s^{-1}, giving a total shear rate range of 6.3 decades. The specifications of the current setup of the FMR are given in Table I.

G. Samples and preparation

All samples used are commercially available complex fluids. The mayonnaise samples labeled "Cains All Natural Mayonnaise" and the fat-free mayonnaise "Cains Fat Free

TABLE I. Parameter range of the flexure-based microgap rheometer for different shearing surface areas

	Gap		Fixture size (surface area)		
	Min: 5 μm	Max: 150 μm	4 mm^2	25 mm^2	225 mm^2
Shear rate ($\dot{\gamma}$)	2×10^{-4} s^{-1}–4×10^{2} s^{-1}	2×10^{-4} s^{-1}–1.4×10^{2} s^{-1}			
Shear stress (τ)			1.1×10^{2} Pa–6.8×10^{5} Pa	1.8×10^{1} Pa–1.1×10^{5} Pa	2.0×10^{0} Pa–1.2×10^{4} Pa
Max. shearing deformation (γ)	320	10			
Sample volume			0.05–1.5 μl	0.2–6.0 μl	1.3–40 μl

Mayonnaise" were produced by Cains Foods, L.P., Ayer, MA 01432. Cains All Natural Mayonnaise, a mayonnaise with 78.6 wt % fat, consisted of soybean oil, water, distilled vinegar, egg yolk, corn syrup, salt, and spices. Cains Fat Free Mayonnaise consisted of water, distilled vinegar, egg white solids, dried onion, garlic juice, oleoresin, paprika, lemon juice, corn syrup, modified food starch, cellulose gel, cellulose gum, xanthan gum, salt, natural flavor, lactic acid, potassium sorbate, sodium benzoate, beta carotene, and calcium disodium edta. All samples were refrigerated before use and transferred directly from the container onto the optical flats that form the lower fixture of the device. The gaps were closed under the action of the approximately constant normal force that arises from the springs of the axial linear nanopositioning stage. No shearing forces were applied during the loading process. The mayonnaise samples were allowed to relax over a period of at least 30 min before the shearing experiments were conducted in order to allow for stress relaxation and recovery of any reversible microstructural deformation during the loading process. The sample volume was chosen to be at least 0.5 ml larger than the required volume to exactly fill the gap and avoid evaporation in the measuring gap.

H. Bulk rheometry

Rheological characterization of bulk samples was carried out on a controlled stress rheometer (AR1000N, TA Instruments, New Castle, DE 19720), using a cone and plate ($\varnothing = 40$ mm, 1°) configuration, and a stress controlled rheometer (AR G2, TA Instruments, New Castle, DE 19720), using a standard plate-and-plate configuration ($\varnothing = 40$ mm). The gap offset error of the plate-and-plate configuration was determined following the procedure described by Kramer *et al.* (Connelly and Greener, 1985; Kramer *et al.*, 1987), by measuring the zero-shear viscosity of a 1 mPas PDMS oil at 16 different separations spanning the range from 1 to 500 μm and then using a linear regression of the inverse apparent zero-shear viscosity as a function of the inverse gap. The gap error of the plate-and-plate configuration was thus determined to be 35.7 ± 0.1 μm. Normal forces arising from the squeeze flow of air in narrow gaps during automated zero-gap determination can result in additional gap errors (Davies and Stokes, 2005). To avoid these additional offset errors, a 10 N normal force criterion for determining the plate and plate contact was chosen, as suggested by Davies and Stokes.

A vane-tool mounted to a Haake RheoStress 1 rotational rheometer (Thermo Electron, Waltham, MA 02454), was also used to determine the yield stress of undisturbed "aged" samples directly in the sample jar.

III. RESULTS AND DISCUSSION

A. Emulsions in small gaps—Mayonnaise

The rheological characterization of foodstuffs and consumer products such as mayonnaise is especially complex because the microscopic structure of an emulsion reaches the dimensions of the flow geometries during the processing and affects the spreading processes of the final product (Rao, 1999). In particular, poorly defined but commercially important parameters such as the difference in "texture" or "mouthfeel" between "full-fat" and "fat-free" products are related to the high shear rates and narrow gaps associated with "mastication" or chewing, and may not be readily measurable in standard bulk rheometry (Giasson *et al.*, 1997). Furthermore, a "natural" emulsion such as that present in Cains All Natural Mayonnaise (i.e., with no artificial surfactants other than the glycerophospholipids of the egg yolk) is very sensitive to de-emulsifying processes and a

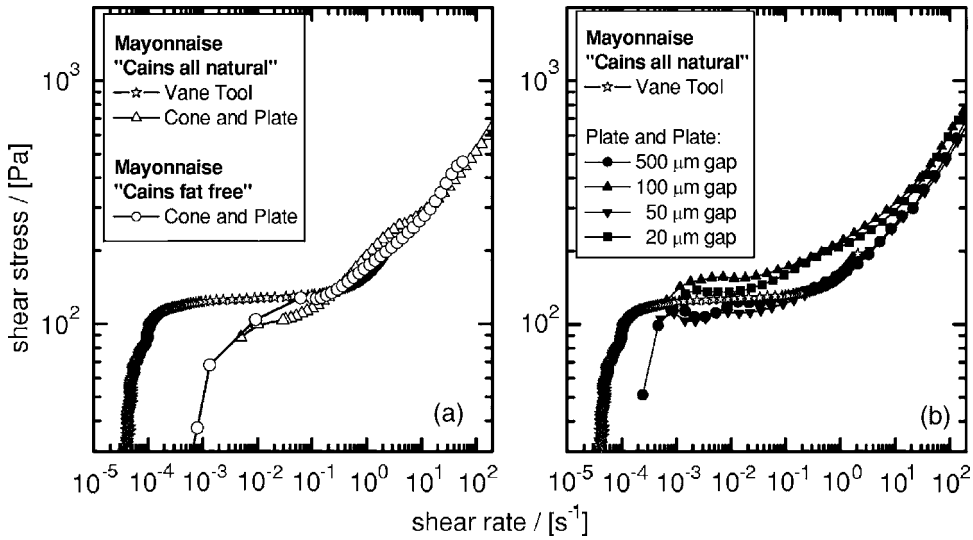

FIG. 6. (a) Comparison of shear stress vs shear rate of natural and fat free mayonnaises, measured with a conventional stress controlled rheometer and a cone-and-plate geometry (∅=4 cm, angle=1°). Also shown are measurements with a vane tool using "undisturbed" or "aged samples" as received in original jars. (b) Shear stress vs shear rate of natural mayonnaise, measured with a plate-and-plate geometry (∅=40 mm) at different gaps. For comparison, the results obtained with the vane tool are also replotted on this graph.

progressive deterioration of quality due to phase separation. Analysis of its mechanical stability under the full range of possible stresses is one of the key features in the production of a consumer-satisfying product.

The flow behavior of mayonnaise has been investigated in detail with conventional bulk rheometers by a number of authors. Although brand-specific differences in composition and manufacturing lead to quantitative differences in the measured material functions, there is broad good agreement about the qualitative flow behavior. Mayonnaise shows a plasticlike response at low shear stresses caused by the network structure of the lipoproteins (Munoz and Sherman, 1990; Gallegos *et al.*, 1992) that is destroyed when the stress exceeds a critical level, leading to a shear yielding of the mayonnaise, a subsequent shear thinning behavior with rising stress (Tiu and Boger, 1974) and time-dependent structural breakdown of the mayonnaise at high stresses (Figoni and Shoemaker, 1983). This overall behavior is also observed for the mayonnaise investigated in this report.

Figure 6(a) shows the shear rate dependence of the stress for Cains All Natural Mayonnaise measured on a conventional rheometer with a cone and plate fixture. The stress first rises with a slope close to unity at low stress in the Newtonian region (corresponding to no microstructural deformation in the mayonnaise and a slow steady creep response), then levels into a broad, plateaulike region corresponding to an apparent yield stress, before finally rising again more slowly in the shear-thinning region. This response is characteristic for many yield stress materials and can be described by phenomenological models such as the Cross model or the Ellis model (Barnes, 1999).

Figure 6(a) also shows the viscometric response for Cains Fat Free Mayonnaise. The data nearly superimpose on the data for the "all natural" mayonnaise; i.e., the real (full-fat) and the fat-free mayonnaise have been formulated to exhibit the same macroscopic shear flow behavior.

Most microstructured products that exhibit a yield stress also show a thixotropic behavior (Stokes and Telford, 2004; Moller *et al.*, 2006); therefore, the loading procedures and waiting time prior to measuring the samples are kept the same for all measurements. Despite these precautions, the yield stresses determined from these measurements still depend weakly on the waiting time and previous deformation history. For comparison, Fig. 6(a) also shows the yield stress of an unsheared mayonnaise sample, determined with a vane tool that is lowered directly into the original 'as received' sample jar. The resulting yield stress level of $\tau_y \approx 130$ Pa is very close to the yield stress level determined from the cone and plate results. It is only the creeping motion below the apparent yield point that exhibits any residual difference between the two tests. This indicates that the chosen waiting time was sufficient to let the mayonnaise samples loaded into the rheometer regain a microstructure that is comparable to that expected in an aged or "non-presheared" sample close to, or above, the yield point.

Figure 6(b) compares the viscometric results for the same mayonnaise obtained using a standard torsional rheometer with a plate-and-plate fixture. The range of gaps utilized is similar to the upper range of plate separations that can be attained with the FMR. Only the data obtained with the largest gap setting of 500 μm at very high shear rates give results that are consistent with the cone and plate fixture. By contrast, measurements with smaller gaps of 100, 50, and 20 μm fail to either reproduce the macroscopic flow curve or to give a reproducible trend that might reflect a progressive microstructural influence on the flow behavior. The radial distribution in deformation rate throughout such shear-sensitive samples makes additional data analysis impossible. Furthermore, even though these measurements have been corrected for the previously determined gap offset error of 39.7 μm, such linear geometric corrections cannot take into account any deviations from a pure shearing deformation that are associated with torsional misalignment of the upper and lower plates. Such "precessing gap error" effects are amplified as the nominal gap setting approaches scales of the order of the gap error, and the additional local biaxial squeezing flow can further alter the sample microstructure.

In contrast to the macroscopic behavior, systematically different flow properties can be observed on the microscopic scale with the FMR. Figure 7 shows the shear-rate-dependent stress for a range of gaps between 95.5 and 7.8 μm. After exhibiting a linear region at low shear rates ($\dot{\gamma} \leqslant 10^{-3}$ s^{-1}) the stress shows a small overshoot with increasing shear rate before leveling into a broad plateau region, corresponding to an apparent yield stress (Barnes, 1999). However, the value of the yield stress in this complex fluid depends on the sample thickness and rises progressively with decreasing gap size. Figure 8 shows the measured dependence of the yield stress on the gap. The yield stress first increases slowly with decreasing gap for gap sizes between 100 and 22 μm, whereas below gap settings of 22 μm, it shows a more rapid increase.

In contrast to this, FMR studies of the fat-free mayonnaise (Cains Fat Free, also shown in Fig. 7) reveal only minor influence of the gap separation on the primary yield stress. The macroscopic shear flow behavior of the fat-free mayonnaise has been successfully formulated to be nearly the same as for a real full-fat mayonnaise; furthermore, the data from the FMR show very similar rheological behavior as in a bulk rheometer.

At higher shear rates the deformation is no longer determined by the yielding process but by a rate-dependent viscometric function. An enlarged view of the measured shear stresses in this region is shown in Fig. 9 and indicates that the stresses increase in a power-law fashion with the shear rate; however, the results do not superpose for different gaps. This behavior is not related to a gap offset error as might be observed in conventional bulk rheometer. Because the gap is determined absolutely with the FMR, these data can be interpreted as an increasing rate of wall slip with rising shear rate above some

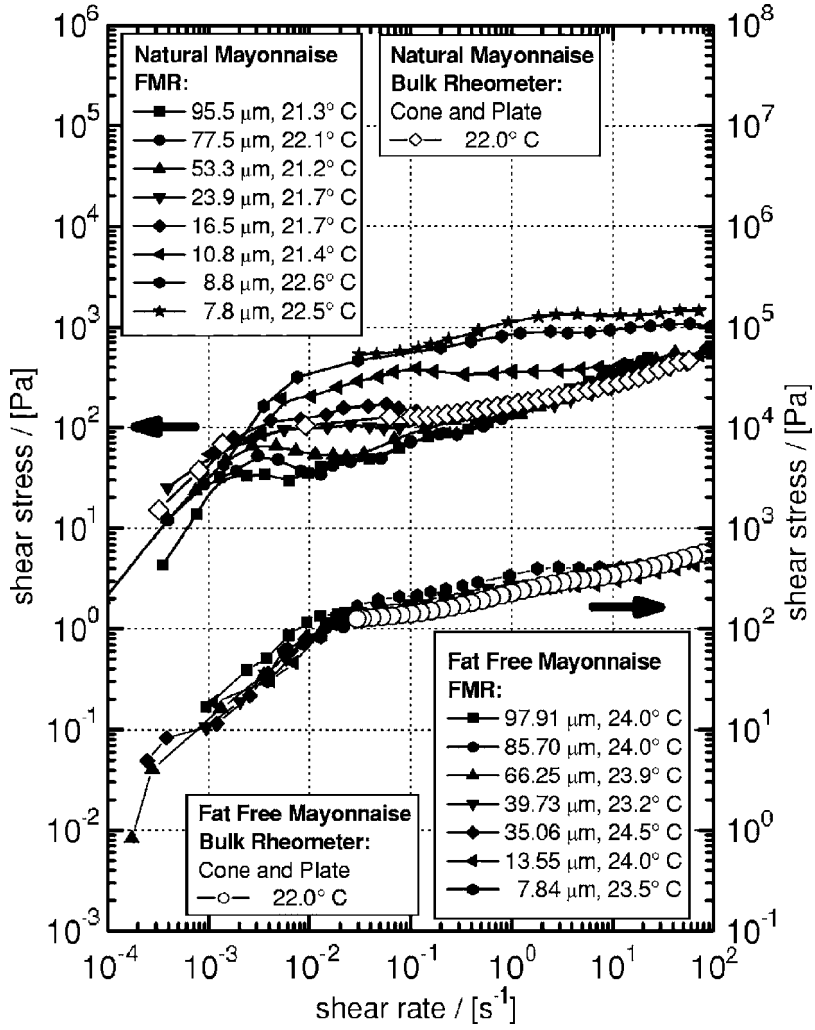

FIG. 7. Flow curves of the shear stress against shear rate for "Cains All Natural" and "Cains Fat Free" mayonnaise measured with the FMR for different gap settings. The open symbols represent the data from rheological characterization of the same samples with a conventional stress controlled rheometer (TA Instruments, AR1000). For clarity the results for the two different samples are presented on different ordinate axes.

critical shear stress, as has been reported previously for mayonnaise at high shear stresses (Ma and Barbosacanovas, 1995; Franco *et al.*, 1998; Goshawk *et al.*, 1998). We use the Mooney method for extracting the thickness of a true slip layer δ at a certain stress (Cohen and Metzner, 1985; Yoshimura and Prudhomme, 1988). The true deformation in the sample consists of two components; a uniform shear rate in the bulk $\dot{\gamma}_b$ and a separate higher shear rate $\dot{\gamma}_w$ in one or more slip layers. For slip layers δ much smaller than the actual gap h the apparent shear rate across the gap is

$$\dot{\gamma} \equiv \frac{U}{h} = \dot{\gamma}_b + \frac{2\delta}{h}\dot{\gamma}_w, \quad \delta \ll h. \tag{3}$$

Linear regression of plots of apparent shear rate as a function of the reciprocal gap for constant values of the shear stress then allows an assessment of the importance of mate-

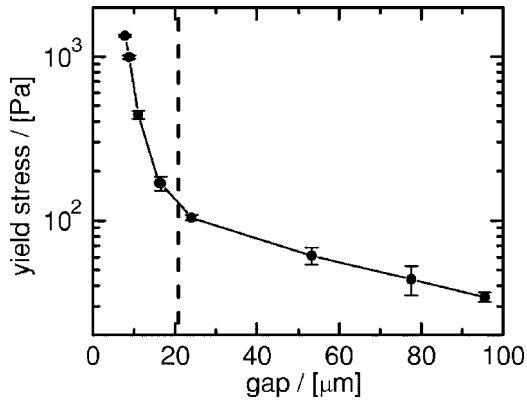

FIG. 8. Yield stress as a function of the gap. Values for the yield stress represent the average value of the overshoot maximum and the following minimum (shown as error bars) from the stress curves in Fig. 7.

rial slip at the wall. Six representative sets of data are shown in Fig. 10(a). The slope of each line is $2\delta\ \dot{\gamma}_w$ and is also known as the slip velocity v_s, i.e., the apparent velocity difference between the wall and the adjacent fluid layer. A common way to represent the effects of slip is in the form of the extrapolation length b that describes the virtual, additional length scale of the gap (Henson and Mackay, 1995). This can also be extracted from the gradients v_s and the y-axis intercepts $\dot{\gamma}_b$ of Fig. 10(a),

$$b = \frac{v_s}{\dot{\gamma}_b} = \frac{2\delta\dot{\gamma}_w}{\dot{\gamma}_b}, \quad \delta \ll h. \tag{4}$$

The resulting extrapolation lengths are shown in Fig. 10(b) and increase linearly with shear stress as expected for a Navier slip law of the form $b=\beta(\tau-\tau_c)$, with $\beta=0.57\ \mu$m/Pa. Assuming that the slip layer consists of a pure water phase (Barnes, 1995; Goshawk *et al.*, 1998), one can also eliminate the wall shear rate in the expression for the slip velocity in favor of the local viscosity of the slip layer ($\dot{\gamma}_w=\tau/\eta_w$) and the

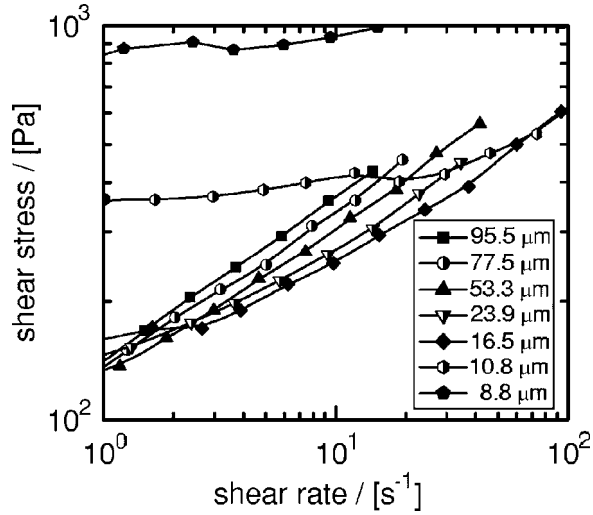

FIG. 9. Enlarged view of the shear thinning region of the viscometric data from Fig. 7.

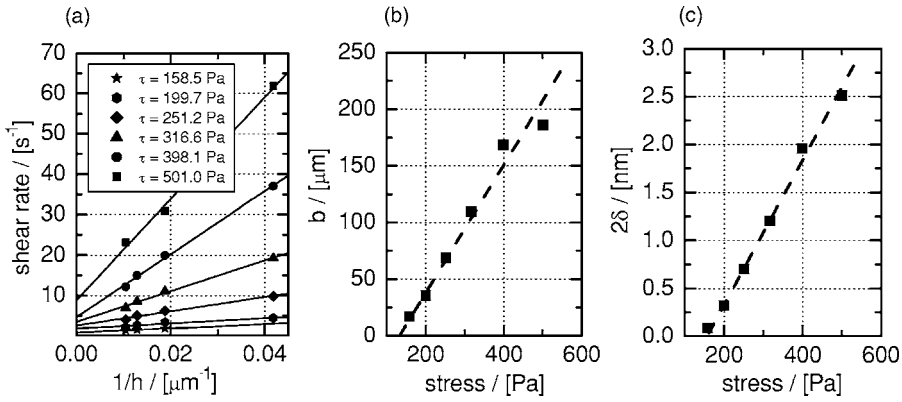

FIG. 10. (a) Apparent shear rate $\dot{\gamma}$ as a function of the reciprocal gap $1/h$ according to Eq. (3), data taken from Fig. 9; (b) extrapolation length b of Eq. (4) as a function of the shear stress τ; (c) determination of the watery slip layer thickness 2δ as a function of the shear stress τ from the gradients $2\delta\dot{\gamma}_w$ of the linear regressions from (a).

wall shear stress. This provides an estimate of the actual slip layer thickness 2δ from the measured slip velocity at a given certain stress τ. The results are shown in Fig. 10(c). Wall slip only occurs above a critical shear stress of $\tau_c \approx 165$ Pa. The thickness 2δ of the watery slip layer(s) is on the order of a few nanometers; however, these experiments do not allow one to determine if the slip occurs on both walls with each layer of thickness δ or in a single layer of thickness 2δ at some undetermined shear band across the sample gap.

Complex microstructural fluids may exhibit several apparent yielding transitions, arising from partial structural breakdown processes during flow at different stress levels, as for example reported by Malkin *et al.* for highly concentrated emulsions (Malkin and Masalova, 2005). In the case of mayonnaise at small gap separations, one can observe a second yielding regime over a range of shear rates $\dot{\gamma}_1 < \dot{\gamma} < \dot{\gamma}_2$ for stresses below the onset of the true wall slip. This is shown in detail in Fig. 11 for two different gap settings (note that separate ordinate axes are used to clearly differentiate the two data sets).

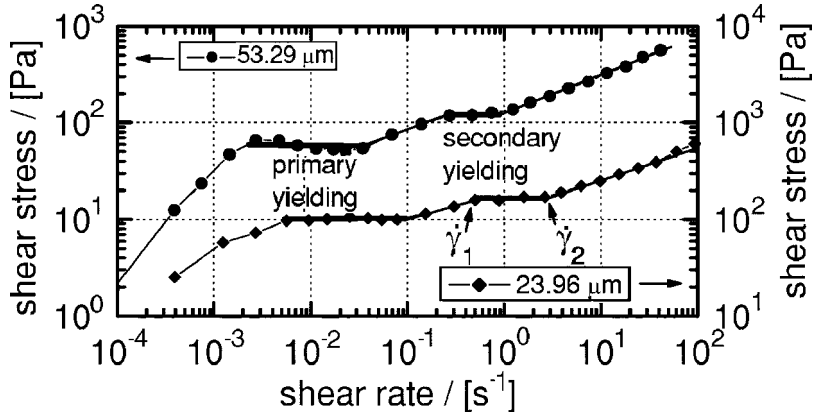

FIG. 11. Primary and secondary yielding for two representative gaps, data taken from Fig. 7. The stress range is shifted for the second curve for a better visualization.

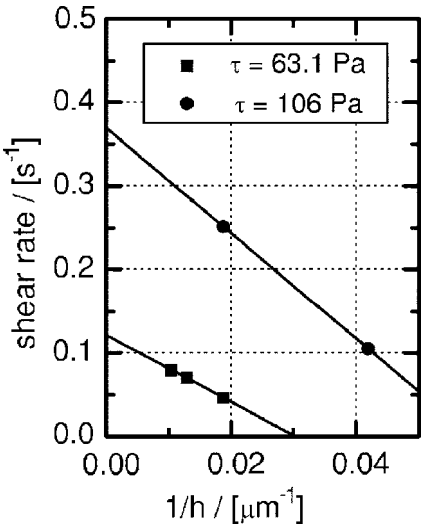

FIG. 12. Apparent shear rate as a function of the reciprocal gap according to Eq. (6).

Simultaneous video microscopic imaging of the motion of discrete oil droplets in the deforming emulsion shows that below the critical shear rate $\dot{\gamma}_2$ single oil droplets close to the walls are not moving, whereas above $\dot{\gamma}_2$ a continuous flow across the gap can be observed. This observation indicates the presence of an unyielded "stick" layer of thickness δ_{stick} at the wall even at stresses above the primary yield stress (Burton *et al.*, 1983). These "sticktion" layers start to yield in the second yielding regime of Fig. 12 once a critical shear stress is exceeded.

Analysis of a wall layer with a viscosity that is different from the bulk and with a thickness that may be on the scale of the overall gap is possible if one modifies Eq. (3) and incorporates a progressive decrease in the thickness of the bulk layer,

$$\dot{\gamma} = \dot{\gamma}_b\left(1 - \frac{2\delta}{h}\right) + \frac{2\delta}{h}\dot{\gamma}_w. \tag{5}$$

Assuming that the shear rate, $\dot{\gamma}_w$, in a stick layer is close to zero, the second term in Eq. (5) can be neglected (Henson and Mackay, 1995), resulting in an apparent shear rate,

$$\dot{\gamma} = \dot{\gamma}_b - \frac{2\delta_{stick}}{h}\dot{\gamma}_b. \tag{6}$$

By analogy to the procedure used for determining the slip layer in Fig. 10, the stick layer thickness δ_{stick} can be determined from the gradient $2\delta_{stick}\dot{\gamma}_b$ in a plot of the shear rate as a function of the reciprocal gap for constant applied shear stresses. Such an analysis is shown in Fig. 12. The stick layer results in an opposite variation with h^{-1} to that observed in the case of wall slip (Fig. 10). For the gap-dependent microrheological data in Fig. 7, this analysis is possible only in a limited number of cases since the linear region observed at stresses below the secondary slip is very often masked by the primary yielding process, especially at lower gaps when the yield stress increases rapidly.

Despite this difficulty, the onset of the secondary yielding regime at the critical shear rate $\dot{\gamma}_1$ where the stick layer δ_{stick} is still intact is typically observable, as can be seen in Fig. 11. In the plateau region of this secondary yielding phenomenon the bulk shear rate $\dot{\gamma}_b$ is expected to be constant; increases in the wall velocity or in the shear stress result in

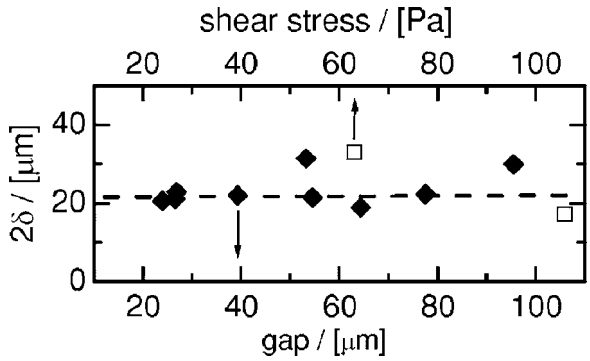

FIG. 13. Thickness of the stick layer $2\delta_{stick}$ as a function of the gap from Eq. (7) (full symbols) and as a function of the stress from Eq. (6) (open symbols.)

progressive disruption of the stationary "sticktion" layer. Assuming that at the end of the secondary yielding regime (shear rate $\dot{\gamma}_2$) the stick layer thickness is zero, one obtains from Eq. (6) that $\dot{\gamma}_1 = \dot{\gamma}_b(1-2\delta_{stick}/h)$ and $\dot{\gamma}_2 = \dot{\gamma}_b$. One can then calculate the stick layer thickness according to the following equation:

$$2\delta_{stick} = \frac{\dot{\gamma}_2 - \dot{\gamma}_1}{\dot{\gamma}_2}. \tag{7}$$

These results for the stick layer thickness are shown in Fig. 13 by the closed symbols. The few results from Fig. 12 for stick layers at two different constant stresses given by $\tau = 63.1$ Pa and $\tau = 106.0$ Pa (corresponding to the data for the largest gaps of $53.3 < h < 95.9$ μm in Fig. 7) are shown as open symbols in Fig. 13. Both results show that the layer thickness is independent of the gap size and has a constant characteristic size of $\sim 21 \pm 2.7$ μm. This is in good agreement with the critical gap distance of 22 μm determined in Fig. 8 for the onset of the dramatic increase of the yield stress. Below this critical gap it is the interaction of the wall stick layers that determines the yielding process in the material, whereas at larger gaps it is the weaker rheological response of the bulk material between the two wall stick layers that dominates the yielding process.

B. "Phase diagram" for microrheology of mayonnaise

We can combine the different measurements of critical stresses for onset of stick/slip transitions and for the magnitude of the yield stress into a "phase diagram" (or more correctly a rheological state diagram) that summarizes the different, gap-dependent classes of response in a complex microstructured fluid such as full-fat mayonnaise. Such a phase diagram is depicted in Fig. 14. The primary yielding transition (full squares, from Fig. 8) and the critical stress at the onset of wall slip [dashed line, determined from Figs. 10(b) and 10(c)] are combined with the values for the secondary yield stresses as a function of the gap (hollow circles, from Fig. 7). If a fixed geometric scale is picked then Fig. 14 summarizes the different modes of rheological response exhibited by this complex fluid. For gaps $\geqslant 25$ μm, four distinct regimes are observed for a chosen fixed value of the gap setting. In regime I, below a gap-dependent primary yield stress (solid squares), the deformation of the material is elastoplastic. The material creeps slowly but the bulk of the deformation is that of an elastic gel. Above this stress in regime II, microrheometry combined with flow visualization shows that there is a localized yielding of the material between two solidlike stick layers that adhere to the shearing surfaces of

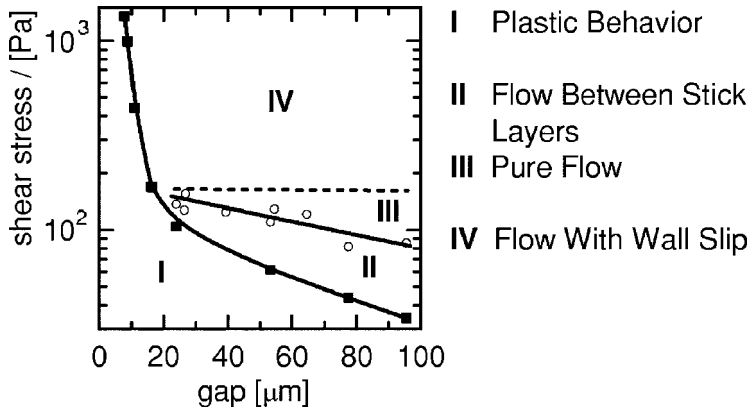

FIG. 14. "Phase diagram" of the gap-dependent flow behavior of mayonnaise, depending on the applied shear stress and the gap separation. The filled symbols (■) refer to the gap-dependent primary yield stress from Fig. 8, the hollow symbols (○) to the secondary yield stress determined from Fig. 7. The dashed line represents the gap-independent critical stress value for onset of wall slip.

the test fixture. Increasing the stress above the secondary yield stress level (hollow symbols) results in the loss of the stick layers and we enter regime III with a pure, continuous, and homogeneous shearing deformation in the sample. A further increase of the shear stress above the gap-independent level corresponding to the critical stress τ_c for onset of wall slip (dashed line) leads into regime IV of bulk flow with wall slip.

It is clear from Fig. 14 that the level of the secondary yield stress resulting from the stick layer converges with the primary yield stress when the gap separation reaches approximately 20 μm. This is consistent with the thickness of the stick layer shown in Fig. 13. An understanding of the nature of this stick layer can be deduced from the microscopic picture of the full-fat mayonnaise shown in Fig. 15(a). Image analysis shows that the largest fat droplets in the emulsion shown in Fig. 15(a) have a dimension of 11–12 μm. These droplet sizes are approximately equal to half of the overall stick layer and therefore correspond to objects that can form a single, rigidlike layer on one wall. The sharp increase in the yield stress below a critical length scale of $\sim$20 μm can therefore be attributed to the onset of direct interactions of the biggest droplets between opposing walls. As the gap closes, compression and/or fusion of these fat droplets together with further additional interactions between smaller droplets lead to the continuous and rapid increase in the yield stress of the emulsion. For comparison, we also show in Fig. 15(b) an image of the microstructure of the fat-free mayonnaise. This image reveals no regular structures having characteristic dimensions on the order of the gap of the FMR which might influence the flow behavior on the microscopic scale. The absence of larger particulate structures was confirmed by analysis of multiple images of other areas of the sample. Consequently the fat-free mayonnaise should not be expected to show a gap dependence in the bulk rheological response, as we have already demonstrated in Fig. 7.

Further increases of the stress in regime IV of Fig. 14 eventually lead to a time-dependent thixotropic flow behavior of the sample. Above a critical stress level, the dispersed phase of the emulsion undergoes a progressive structural change with continual shearing and breaks down into smaller droplets until a new, stable emulsion structure is reached. A rough estimate of the critical stress at which the droplets will eventually start to break up can be obtained by considering the capillary number of the flow field around the droplets,

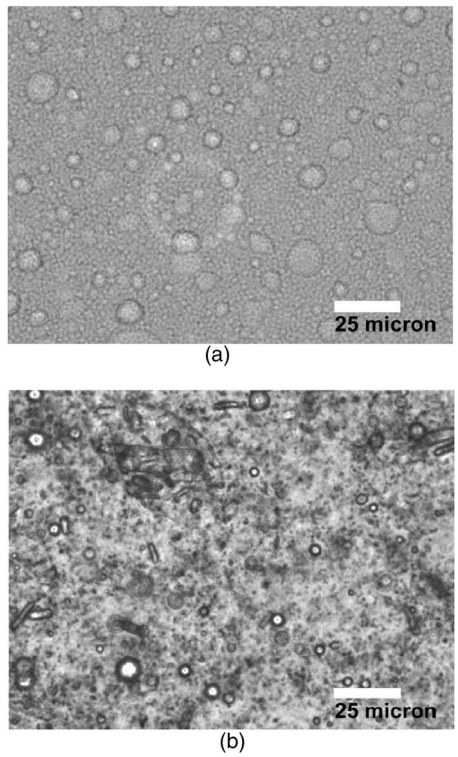

FIG. 15. Microscopic view under bright field illumination of (a) the real full-fat mayonnaise sample and (b) of the fat-free mayonnaise. The view direction is perpendicular to the gap. The white line corresponds to a 25 μm scale bar.

$$Ca = \frac{\tau}{\sigma/R}, \tag{8}$$

where σ is the interfacial tension. For vegetable oil in water emulsions with a viscosity ratio $\mu_{drop}/\mu_{cont} \sim 2$ a critical capillary number Ca_{cr} for the onset of droplet breakup in steady shear flow is $Ca_{cr} \approx 0.45$ (Guido and Greco, 2004). The interfacial tension of egg yolk stabilized vegetable oil in water emulsions is reported to be $\sigma \approx 8$ mN/m (Mel'nikov, 2002). Combining this value with the observed radius of the larger droplets ($R \sim 6$ μm), we obtain an estimate of a critical stress level of $\tau_{cr} \simeq 0.45(\sigma/R) = 600$ Pa. Above this stress level structural degradation of the emulsion is expected.

However, the current configuration of the FMR enables us to perform only *controlled rate* experiments, and it is therefore not possible to set a defined, constant stress level to probe the stability of the emulsion above this critical stress level τ_{cr}. We therefore set a constant, high shear rate that generates an initial stress level of 800 Pa in the full-fat mayonnaise, well above the theoretical critical stress level τ_{cr}, and follow the evolution of the stress over time as demonstrated in Fig. 16. Simultaneous videomicroscopic imaging of the emulsion structure then enables a direct correlation of the microstructural changes with the stress state.

We cannot follow clearly the dimensional change of single droplets of the dispersed phase, since the spatial resolution of the videomicroscopic images is not high enough. However, the relative density of oil droplets can still be obtained from an analysis of the

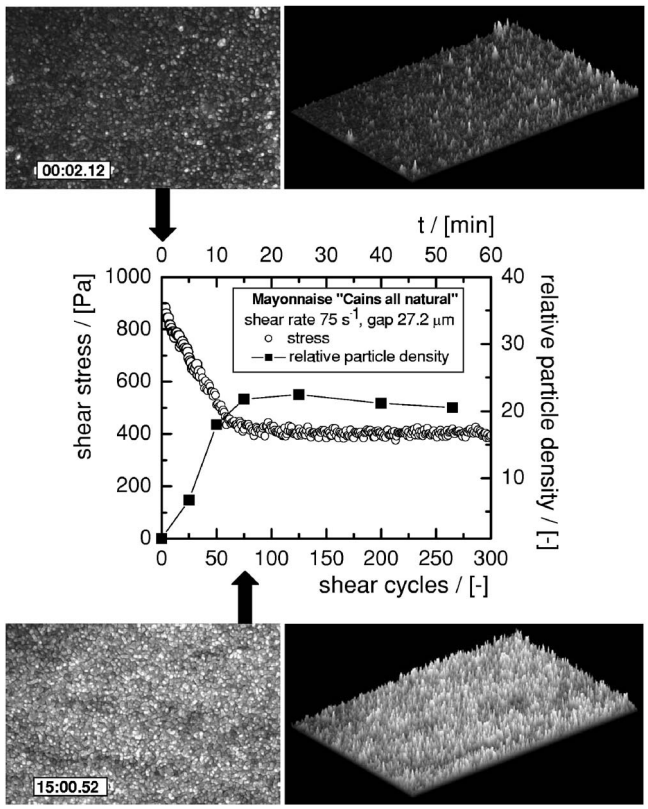

FIG. 16. Temporal evolution of shear stress under steady shearing at a high shear rate of 75 s^{-1} with a gap of 27.2 μm for full-fat mayonnaise. In addition, the evolution in the relative density of scattering droplets, scaled with the initial value at $t=0$, is given, determined from video-microscopic images of the upper, quasistationary shearing surface, as shown on the left-hand side. The images on the right-hand side show three-dimensional representations of the intensity level of individual scattering centers.

intensity variations of the video images as shown in Fig. 16. The number density of scattering centers above an arbitrary intensity threshold level at a time t, scaled by the number density at $t=0$, gives a relative measure of the increase in the number of dispersed droplets over time. This relative number density increases over 15 min for the chosen shear rate in Fig. 16 ($\dot{\gamma}=75\ s^{-1}$) and then levels at a constant value that is approximately 22 times higher then the initial value. At the same time the measured stress decreases steadily during the first 15 min, in accordance with the progressive droplet breakdown, and then also plateaus at a new constant value.

It is clear from these observations that there is another transition in the phase diagram of Fig. 14 that represents the onset of a thixotropic regime V. However, neither the dependence of the final, stable stress level in Fig. 16 on the initial imposed stress level, nor the dependence on the gap or the reversibility of this microstructural change after cessation of stress has been explored in the present study and remains the subject of future investigations.

IV. DISCUSSION AND CONCLUSIONS

In this paper we have outlined the design, construction, and validation of a new flexure-based microrheometry system. This device may perhaps be best considered as a

miniaturized version of the sliding plate rheometer pioneered by Dealy and co-workers (Giacomin *et al.*, 1989). Like the sliding plate device it generates a plane Couette flow in a sample and uses a displacement-based transduction system to monitor the shear stress acting on one of the shearing surfaces. The use of a compound flexure allows large deformations corresponding to a shear strain of up to $\gamma=200$ to be imposed on samples. By merging this design with nanostepping motors for alignment of the fixtures and a white light interferometry system for absolute gap determination we are able to generate homogeneous deformations over a wide range of stresses and strain rates.

We have used this rheometer to study the gap dependence and shear-rate dependence of a typical microstructured consumer food product: mayonnaise. This natural oil/water emulsion exhibits a strong gap dependence in its viscometric properties when the gap separation approaches the characteristic length scale of the internal microstructure. Experiments at different gap settings and different shear rates coupled with direct digital imaging of the flow enable us to construct a phase diagram or rheological state diagram in terms of the shear stress acting on the fluid and the gap that constrains the microstructure. The resulting diagram (shown in Fig. 14) enables us to understand how the material will deform and flow under different conditions (for example in processing equipment or, ultimately, in the mouth). It is worth noting from Fig. 14 that the boundaries which demarcate several of the different flow regimes appear to converge at a single critical point in this state space (like the "triple point" of a simple liquid). These critical values, $\tau_c \approx 160$ Pa, and $h_c \approx 20$ μm, can be combined with the published value of the surface tension of a natural egg yolk-based mayonnaise, $\sigma=8.0$ mN/m (Mel'nikov, 2002) to understand the competition between the imposed shear stress and the internal capillary pressure of the fluid. The corresponding capillary number at this critical point is $Ca_c=\tau_c h_c/\sigma \approx 0.4$. There thus appears to be a strong connection between the conditions at the critical point and Grace's original investigations of shear-induced rupturing of isolated drops in an unbounded shear flow (see Guido and Greco, 2004 for a recent review). Similar phase diagrams can also be constructed for other complex consumer products such as creams and lotions (Clasen and McKinley, 2004), although in such multicomponent systems it is less easy to connect the individual transitions with specific flow transitions or microstructural deformations.

The formulation of the natural emulsion studied in this paper can also be modified by replacing some, or all, of the fat droplets with a fibrous biopolymeric filler. Although it is possible to match the apparent rheological properties on the macroscale, our measurements show that the resulting fat-free product behaves significantly differently from the full-fat emulsion at small gaps and high shear rates. It would be interesting in the future to correlate such differences with consumer assessment of perceptual properties such as texture and mouthfeel.

At the present time, the flexure-based microrheometer system is limited to experiments at room temperature. However, in principle, Peltier elements could be mounted on the back faces of the optical flats that form the shearing surfaces, or alternately the entire apparatus could be mounted in a controlled-temperature environment. In addition, by mounting a second compound flexure at 90° to the upper fixture shown in Fig. 2, it is possible to measure and control normal displacement of the fixtures. By coupling this normal displacement with a voice coil or other variable force actuator it would be possible to construct a force-rebalance system for measuring normal stress differences. Although complex, a normal-force-controlled flexure system of this type has recently been built for microtribological testing of polymeric samples (Gudlavalleti *et al.*, 2005).

The FMR device requires very small volumes of fluid (0.1–20 μl). Therefore, in addition to the ability to probe the gap dependence of viscometric properties in complex

fluids such as foods and other consumer products, it can also be of use as a microrheometer when only very small volumes of test fluid are available. This is often the case when studying the properties of natural and synthetic biopolymeric materials such as mucins, silks, or custom-designed peptide gels. Although it is already possible to measure the linear viscoelastic properties of such materials using bead-based microrheometry, the FMR is able to impose sufficiently large shear stresses to induce yielding of the microstructure and then measure the resulting flow properties in steady and time-varying shear flows. We hope to report further on such systems in the future.

ACKNOWLEDGMENTS

The authors would like to thank Professor L. Anand, MIT, for his kind support with the design of the compound spring. The authors would also like to acknowledge the Dupont MIT Alliance (DMA) for financial support during the construction of the FMR.

References

Barnes, H. A., "A review of the slip (wall depletion) of polymer-solutions, emulsions and particle suspensions in viscometers—Its cause, character, and cure," J. Non-Newtonian Fluid Mech. **56**, 221–251 (1995).

Barnes, H. A., "The yield stress—a review or 'pi alpha nu tau alpha rho epsilon iota'—everything flows?" J. Non-Newtonian Fluid Mech. **81**, 133–178 (1999).

Bausch, A. R., F. Ziemann, A. A. Boulbitch, K. Jacobson, and E. Sackmann, "Local measurements of viscoelastic parameters of adherent cell surfaces by magnetic bead microrheometry," Biophys. J. **75**, 2038–2049 (1998).

Braithwaite, G. J. C., and G. H. McKinley, "Microrheometry for studying the rheology and dynamics of polymers near interfaces," Appl. Rheol. **9**, 27–33 (1999).

Burton, R. H., M. J. Folkes, K. A. Narh, and A. Keller, "Spatial variation in viscosity in sheared polymer melts," J. Mater. Sci. **18**, 315–320 (1983).

Clasen, C., and G. H. McKinley, "Gap-dependent microrheometry of complex liquids," J. Non-Newtonian Fluid Mech. **124**, 1–10 (2004).

Cohen, Y., and A. B. Metzner, "Apparent slip-flow of polymer solutions," J. Rheol. **29**, 67–102 (1985).

Connelly, R. W., and J. Greener, "High-shear viscometry with a rotational parallel-disk device," J. Rheol. **29**, 209–226 (1985).

Davies, G. A., and J. R. Stokes, "On the gap error in parallel plate rheometry that arises from the presence of air when zeroing the gap," J. Rheol. **49**, 919–922 (2005).

Dhinojwala, A., and S. Granick, "Micron-gap rheo-optics with parallel plates," J. Chem. Phys. **107**, 8664–8667 (1997).

Figoni, P. I., and C. F. Shoemaker, "Characterization of time-dependent flow properties of mayonnaise under steady shear," J. Texture Stud. **14**, 431–442 (1983).

Franco, J. M., C. Gallegos, and H. A. Barnes, "On slip effects in steady-state flow measurements of oil-in-water food emulsions," J. Food. Eng. **36**, 89–102 (1998).

Gallegos, C., M. Berjano, and L. Choplin, "Linear viscoelastic behavior of commercial and model mayonnaise," J. Rheol. **36**, 465–478 (1992).

Gardel, M. L., M. T. Valentine, and D. A. Weitz, "Microrheology," in *Microscale Diagnostic Techniques*, edited by K. Breuer, (Springer, Berlin, 2005) pp. 1–50.

Gearing, B. P., and L. Anand, *ASME Int. Mech. Eng. Congress and Exposition*. New York, NY (2001).

Giacomin, A. J., T. Samurkas, and J. M. Dealy, "A novel sliding plate rheometer for molten plastics," Polym. Eng. Sci. **29**, 499–504 (1989).

Giasson, S., J. Israelachvili, and H. Yoshizawa, "Thin film morphology and tribology study of mayonnaise," J. Food. Sci. **62**, 640–652 (1997).

Goshawk, J. A., D. M. Binding, D. B. Kell, and R. Goodacre, "Rheological phenomena occurring during the shearing flow of mayonnaise," J. Rheol. **42**, 1537–1553 (1998).

Gosse, C., and V. Croquette, "Magnetic tweezers: Micromanipulation and force measurement at the molecular level," Biophys. J. **82**, 3314–3329 (2002).

Gudlavalleti, S., B. P. Gearing, and L. Anand, "Flexure-based micromechanical testing machines," Exp. Mech. **45**, 412–419 (2005).

Guido, S., and F. Greco, "Dynamics of a liquid drop in a flowing immiscible liquid," in *Rheology Reviews*, edited by D. M. Binding and K. Walters (British Society of Rheology, Aberystwyth, 2004), pp. 99–142.

Henson, D. J., and M. E. Mackay, "Effect of gap on the viscosity of monodisperse polystyrene melts—Slip effects," J. Rheol. **39**, 359–373 (1995).

Israelachvili, J. N., and D. Tabor, "Measurement of van der Waals dispersion forces in the range 1.5 to 130 nm," Proc. R. Soc. London, Ser. A **331**, 19–38 (1972).

Israelachvili, J. N., P. M. McGuiggan, and A. M. Homola, "Dynamic properties of molecularly thin liquid-films," Science **240**, 189–191 (1988).

Kramer, J., J. T. Uhl, and R. K. Prudhomme, "Measurement of the viscosity of guar gum solutions to 50,000 1/s using a parallel plate rheometer," Polym. Eng. Sci. **27**, 598–602 (1987).

Levine, A. J., and T. C. Lubensky, "One- and two-particle microrheology," Phys. Rev. Lett. **85**, 1774–1777 (2000).

Ma, L., and G. V. Barbosacanovas, "Rheological characterization of mayonnaise. I. Slippage at different oil and xanthan gum concentrations," J. Food. Eng. **25**, 397–408 (1995).

MacKintosh, F. C., and C. F. Schmidt, "Microrheology," Curr. Opin. Colloid Interface Sci. **4**, 300–307 (1999).

Malkin, A. Y., and I. Masalova, "Rheology of Super-Concentrated Emulsions," at 4th Pacific Rim Conference on Rheology, Shanghai, China (2005).

Meiners, J. C., and S. R. Quake, "Femto-Newton force spectroscopy of single extended DNA molecules," Phys. Rev. Lett. **84**, 5014–5017 (2000).

Mel'nikov, S. M., "Effect of pH on the adsorption kinetics of egg yolk at the triacylglycerol-water interface and viscoelastic properties of interfacial egg yolk films: A dynamic drop tensiometry study," Colloids Surf., B **27**, 265–275 (2002).

Mhetar, V., and L. A. Archer, "Slip in entangled polymer solutions," Macromolecules **31**, 6639–6649 (1998).

Migler, K. B., H. Hervet, and L. Leger, "Slip transition of a polymer melt under shear-stress," Phys. Rev. Lett. **70**, 287–290 (1993).

Moller, P. C. F., J. Mewis, and D. Bonn, "Yield stress and thixotropy: On the difficulty of measuring yield stresses in practice," Soft Mater. **2**, 274–283 (2006).

Montfort, J. P., A. Tonck, J. L. Loubet, and J. M. Georges, "Microrheology of high-polymer solutions," J. Polym. Sci., Part B: Polym. Phys. **29**, 677–682 (1991).

Mukhopadhyay, A., and S. Granick, "Micro- and nanorheology," Curr. Opin. Colloid Interface Sci. **6**, 423–429 (2001).

Munoz, J., and P. Sherman, "Dynamic viscoelastic properties of some commercial salad dressings," J. Texture Stud. **21**, 411–426 (1990).

Popescu, G., A. Dogariu, and R. Rajagopalan, "Spatially resolved microrheology using localized coherence volumes," Phys. Rev. E **65**, 041504 (2002).

Raghu, A., and S. Ananthamurthy, "Construction of an optical tweezer for nanometer scale rheology," Pramana, J. Phys. **65**, 699–705 (2005).

Rao, M. A., *Rheology of Fluid and Semisolid Foods* (Aspen Publishers, Gaithersburg, MD, 1999).

Reimers, M. J., and J. M. Dealy, "Sliding plate rheometer studies of concentrated polystyrene solutions: Nonlinear viscoelasticity and wall slip of two high molecular weight polymers in tricresyl phosphate," J. Rheol. **42**, 527–548 (1998).

Soga, I., A. Dhinojwala, and S. Granick, "Optorheological studies of sheared confined fluids with mesoscopic thickness," Langmuir **14**, 1156–1161 (1998).

Starrs, L., and P. Bartlett, "One- and two-point micro-rheology of viscoelastic media," J. Phys.: Condens. Matter **15**, S251–S256 (2003).

Stokes, J. R., and J. H. Telford, "Measuring the yield behaviour of structured fluids," J. Non-Newtonian Fluid

Mech. **124**, 137–146 (2004).

Tiu, C., and D. V. Boger, "Complete rheological characterization of time-dependent food products," J. Texture Stud. **5**, 329–338 (1974).

Waigh, T. A., "Microrheology of complex fluids," Rep. Prog. Phys. **68**, 685–742 (2005).

Weitz, D. A., and D. J. Pine, "Diffusing Wave Spectroscopy," in *Dynamic Light Scattering*, edited by W. Brown (Oxford University Press, Oxford, 1992).

Yoshimura, A., and R. K. Prudhomme, "Wall slip corrections for couette and parallel disk viscometers," J. Rheol. **32**, 53–67 (1988).